JACS
JOURNAL OF THE AMERICAN CHEMICAL SOCIETY
pubs.acs.org/JACS
Article

Sequential Spin State Transition and Intermetallic Charge Transfer in $PbCoO_3$

Zhehong Liu, Yuki Sakai, Junye Yang, Wenmin Li, Ying Liu, Xubin Ye, Shijun Qin, Jinming Chen,* Stefano Agrestini, Kai Chen, Sheng-Chieh Liao, Shu-Chih Haw, Francois Baudelet, Hirofumi Ishii, Takumi Nishikubo, Hayato Ishizaki, Tatsuru Yamamoto, Zhao Pan, Masayuki Fukuda, Kotaro Ohashi, Kana Matsuno, Akihiko Machida, Tetsu Watanuki, Saori I. Kawaguchi, Angel M. Arevalo-Lopez, Changqing Jin, Zhiwei Hu, J. Paul Attfield, Masaki Azuma,* and Youwen Long*

Cite This: *J. Am. Chem. Soc.* 2020, 142, 5731−5741

Read Online

ACCESS | Metrics & More | Article Recommendations | Supporting Information

ABSTRACT: Spin state transitions and intermetallic charge transfers can essentially change material structural and physical properties while excluding external chemical doping. However, these two effects have rarely been found to occur sequentially in a specific material. In this article, we show the realization of these two phenomena in a perovskite oxide $PbCoO_3$ with a simple ABO_3 composition under high pressure. $PbCoO_3$ possesses a peculiar A- and B-site ordered charge distribution $Pb^{2+}Pb^{4+}{}_3Co^{2+}{}_2Co^{3+}{}_2O_{12}$ with insulating behavior at ambient conditions. The high spin Co^{2+} gradually changes to low spin with increasing pressure up to about 15 GPa, leading to an anomalous increase of resistance magnitude. Between 15 and 30 GPa, the intermetallic charge transfer occurs between Pb^{4+} and Co^{2+} cations. The accumulated charge-transfer effect triggers a metal−insulator transition as well as a first-order structural phase transition toward a Tetra.-I phase at the onset of ∼20 GPa near room temperature. On further compression over 30 GPa, the charge transfer completes, giving rise to another first-order structural transformation toward a Tetra.-II phase and the reentrant electrical insulating behavior.

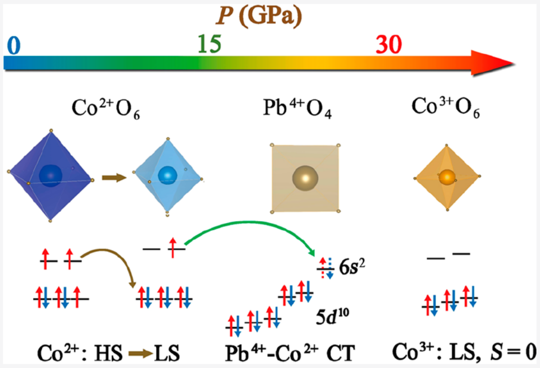

1. INTRODUCTION

Transition-metal oxides exhibit a wide variety of intriguing physical properties and versatile functionalities such as ferroelectricity, ferromagnetism, catalysis, superconductivity, colossal magnetoresistance, magnetoelectric multiferroicity, etc.[1−9] All these properties are closely related to the d-electron configurations of transition metals which involve the number of unpaired d-electrons as well as the detailed electronic distributions at different orbitals. Chemical substitution is a widely used method to modify the electronic configurations and thereby manipulate materials structures and properties. However, the external element doping may inevitably cause some inhomogeneous chemical disorders, which are unfavorable to understanding the intrinsic physical properties. On the other hand, there exist some "internal" effects that can also change the electronic configurations without the introduction of any doping element. A spin state transition is a typical example of one of these effects. As is well-known, on heating, the spin state of Co^{3+} in $LaCoO_3$ gradually changes from low spin (LS) to high spin (HS) via a possible intermediate spin (IS) state, accompanied by magnetic and electrical transport variations.[10−17] Some other compounds containing Mn, Fe, and Co also show spin state transitions by changing the environment conditions such as temperature, pressure, and/or light radiation, etc.[18−26]

Intermetallic charge transfer is a more interesting manner to change the electronic configurations without introducing external element. In sharp contrast to spin state transitions, which only change the electronic states for a single cation, intermetallic charge transfer takes place between two different metals so that much more drastic variations in structure, magnetism, and electrical transport properties are expected to jointly occur. Compared with a spin state transition, intermetallic charge transfer is only observed in a few transition-metal oxides. An interesting example is $LaCu_3Fe_4O_{12}$, where Cu−Fe intermetallic charge transfer occurs on heating to 393 K or pressuring to 3.6 GPa at room

Received: December 16, 2019
Published: February 21, 2020

temperature (RT), resulting in the change of charge combination from $LaCu^{3+}_3Fe^{3+}_4O_{12}$ to $LaCu^{2+}_3Fe^{3.75+}_4O_{12}$ accompanied by insulator-to-metal and antiferromagnetism-to-paramagnetism transformations as well as the presence of negative thermal expansion.[27,28] Similarly, intermetallic charge transfer is also observed in $BiNiO_3$ between Bi and Ni, causing the charge format change from $Bi^{3+}{}_{0.5}Bi^{5+}{}_{0.5}Ni^{2+}O_3$ to $Bi^{3+}Ni^{3+}O_3$.[29]

Although spin state transition and intermetallic charge transfer have received much attention in the past, these two phenomena rarely occur together in a specific material. The only report is in a perovskite oxide family with a complicated composition $(Pr_{1-x}R_x)_{0.7}Ca_{0.3}CoO_3$ (R = Y, Sm) composed of mixed Co^{3+}/Co^{4+} and Pr^{3+}/Pr^{4+} states.[30−36] The high-pressure synthesized perovskite oxide $PbCoO_3$ provides a unique opportunity for such a discovery in a compound with a simple ABO_3 composition. On account of the peculiar A- and B-site charge orderings, $PbCoO_3$ crystallizes in an $AA'_3B_2B'_2O_{12}$-type quadruple perovskite structure (Figure 1) with the charge combination of $Pb^{2+}Pb^{4+}{}_3Co^{2+}{}_2Co^{3+}{}_2O_{12}$, where the Co^{2+} is confirmed to be HS with the spin value $S = 3/2$ while Co^{3+} is LS with $S = 0$.[37] The former has a magnetic frustration owing to the tetrahedral arrangement and orders antiferromagnetically below 7.8 K. HS Co^{2+} is sensitive to external stimuli like high pressure, at which a HS-to-LS transition is highly likely to occur, as observed in CoO and other Co^{2+}(HS)-containing compounds.[18,38] In addition, the 6s states of Pb have similar energy levels as those of the d orbitals of Co.[37] As a result, moderate stimuli may also trigger the Pb−Co intermetallic charge transfer, causing different charge combination and physical properties.[37,39] In this paper, we report the realization of both spin state transition and intermetallic charge transfer accompanied by double metal−insulator and crystal structure phase transitions in $PbCoO_3$ as evidenced by a series of *in situ* high-pressure measurements including electrical transport, neutron diffraction, synchrotron X-ray diffraction, emission, and absorption spectroscopies.

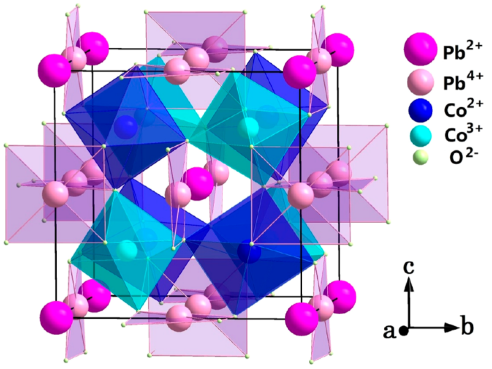

Figure 1. Schematic crystal structure of both A- and B-site ordered $PbCoO_3$ ($Pb^{2+}Pb^{4+}{}_3Co^{2+}{}_2Co^{3+}{}_2O_{12}$) quadruple perovskite with $Pn\bar{3}$ symmetry. The corner-sharing $Co^{2+}/Co^{3+}O_6$ octahedra and isolated $Pb^{4+}O_4$ squares are shown. Atomic positions are the following: Pb^{2+} 2*a* (0.5, 0.5, 0.5), Pb^{4+} 6*d* (0.5, 0, 0), Co^{2+} 4*b* (0.25, 0.25, 0.25), Co^{3+} 4*c* (0.75, 0.75, 0.75), O^{2-} 24*h* (*x*, *y*, *z*).

2. METHODS SECTION

Polycrystalline $PbCoO_3$ samples were prepared at high pressure and high temperature conditions as reported before.[37] High purity (>99.9%) PbO, PbO_2, and Co_3O_4 starting materials with a mole ratio of 1:2:1 were well mixed in an agate mortar. The mixed powders were then pressed into a gold capsule with 3 mm in diameter and length for further treatment at 12 GPa and 1323 K for 30 min using a Walker-type multianvil high pressure apparatus. When the heating time was finished, the sample was quenched to room temperature, and then the pressure was slowly released to ambient pressure. X-ray powder diffraction was performed to identify the sample quality using a Huber diffractometer (Cu $K\alpha_1$ radiation, 40 kV, 30 mA).

The electronic transport properties of $PbCoO_3$ at high pressure were measured using the standard four-probe method with a screw type diamond anvil cell (DAC) made of nonmagnetic Be−Cu alloy as described elsewhere.[40] The diamond culet was 300 μm in diameter, and a T301 stainless steel gasket was preindented from 250 to 40 μm thickness with a center hole of 150 μm in diameter. The gasket was then covered by cubic BN fine powders to be the insulating layer that, drilled with a 80 μm diameter hole, served as sample chamber. The $PbCoO_3$ fine powders pressed with a dimension of $50 \times 50 \times 10$ μm^3 were loaded with soft NaCl fine powder surrounding as pressure transmitting medium. We used a slim Au wire of 18 μm diameter as electrodes. Pressures were calibrated by ruby fluorescence shift method for all the DAC-related experiments used in this paper.[41] The DAC was placed inside a Mag-Lab system to perform the experiments. A thermometer located around the sample in the DAC was used for monitoring the sample temperature.

High-pressure synchrotron X-ray emission spectroscopy (XES) and X-ray absorption spectroscopy (XAS) results were obtained using DAC techniques at RT. The pressure dependent Co K XAS spectra were measured at the ODE beamline of the synchrotron SOLEIL, France. The Co-metal foil was used as reference for the cobalt chemical shift. The high pressure Co K_β X-ray emission spectra with an overall resolution of ∼0.9 eV and high resolution partial fluorescence yield Pb L_3 XAS spectra measured at the Pb $L_{\alpha1}$ emission line with an overall resolution of ∼2.5 eV were obtained at the Taiwan inelastic X-ray scattering BL12XU beamline at SPring-8 in Japan. The Co K_β X-ray emission and Pb $L_{\alpha1}$ emission signals were analyzed with a spectrometer (Johann type) equipped with a spherically bent Ge(444) crystal and Si(555) (radius 1 m), respectively, arranged on a horizontal plane in a Rowland-circle geometry. The strong X-ray absorption of Pb ion leads to relative large error bar in Co K_β X-ray emission spectra of $PbCoO_3$ as compared with that of $SrCo_{0.5}Ru_{0.5}O_3$.[42]

The high-pressure synchrotron X-ray diffraction (SXRD) experiment was performed at beamline BL22XU in SPring-8 by using DACs with rhenium and stainless-steel gaskets. Helium was used as a pressure medium. The wavelengths of 0.4964 and 0.4961 Å were used in the room- and low-temperature experiments, respectively. The RIETAN-FP program was used to analyze the SXRD data.[43] Time-of-flight neutron powder diffraction (NPD) data at high pressure and RT conditions were recorded with the instrument PEARL/HiPr at the ISIS facility, U.K. About 90 mm^3 of the sample was loaded into a Paris−Edinburgh cell[44] with 4:1 methanol−ethanol as a pressure medium and a small pellet of lead as the pressure calibration. Rietveld profile refinements of the structural models were performed with the GSAS software.[45]

3. RESULTS AND DISCUSSION

Figure 1 shows the schematic crystal structure for the quadruple perovskite oxide $Pb^{2+}Pb^{4+}{}_3Co^{2+}{}_2Co^{3+}{}_2O_{12}$ with space group $Pn\bar{3}$ at ambient conditions. In this crystal symmetry, the Pb^{2+} and Pb^{4+} are 1:3 ordered at the A and A′ sites, forming $Pb^{2+}O_{12}$ and square-planar $Pb^{4+}O_4$ coordinated units, respectively. In spite of the smaller charge difference, the large discrepancy of ionic radius between the HS $Co^{2+}(t_{2g}{}^5e_g{}^2)$ and the LS $Co^{3+}(t_{2g}{}^6e_g{}^0)$ makes them ordered at the octahedral coordinated B/B′ sites with a rocksalt-type manner. This is similar to that observed in $La_{1.5}Sr_{0.5}CoO_4$, where the hopping of charge carries between these two types of Co ions is confirmed to be severely suppressed due to the

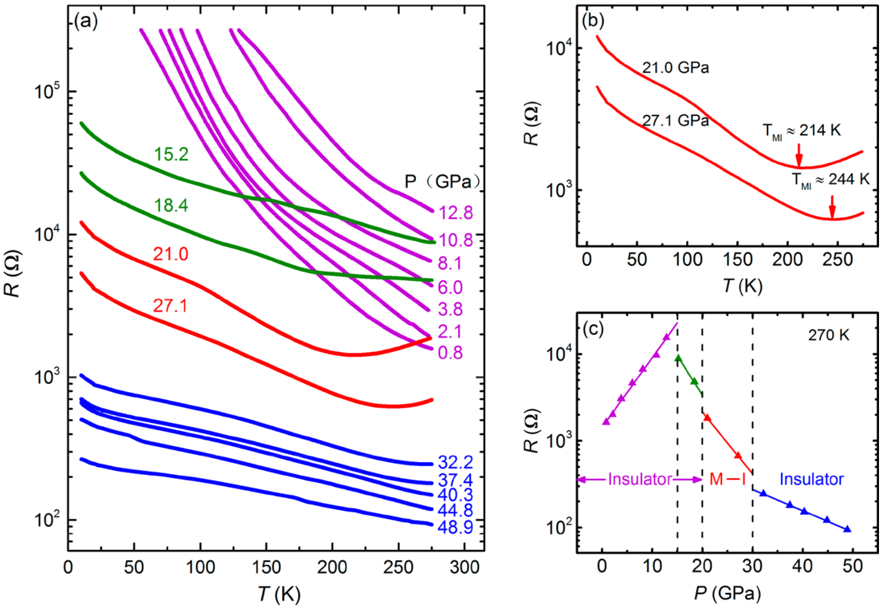

Figure 2. Electrical transport properties of $PbCoO_3$. (a) Temperature-dependence of resistance at different pressures. (b) Metal−insulator transitions observed at 21.0 and 27.1 GPa. The T_{MI} stands for the critical temperature for the transition. (c) Resistance values under various pressures at 270 K. The triangles show the measurement data, and the lines display the linear fitting results.

spin-blockade effect.[46] $PbCoO_3$ thus also shows electrical insulating behavior at ambient pressure. For most 3d transition-metal oxides, applying physical pressure can often enhance the p−d hybridization and extend the d-electron bandwidth. As a consequence, the resistance under high pressure is expected to decrease. In sharp contrast, however, the resistance of $PbCoO_3$ gradually increases as the pressure raises from 0.8 to 12.8 GPa, as shown in Figure 2a. This unusual feature can be attributed to the continuous spin state transition of Co^{2+} from high spin to low spin, as will be further confirmed by synchrotron XES and NPD studies. Once the HS Co^{2+} to LS transition is complete, the electronic configuration will vary from $t_{2g}^5e_g^2$ to $t_{2g}^6e_g^1$. In the Co^{2+}/Co^{3+}-site rocksalt-type ordered crystal structure, electron hopping between the low-spin Co^{2+} and Co^{3+} is also forbidden, or the ordered structure will be broken into a disordered one. Our SXRD reveals that the A- and B-site ordered $Pn\overline{3}$ structure of $PbCoO_3$ is unchanged up to ∼20 GPa near RT (shown later). Since the possible carrier hopping via the Co^{2+}−O−O−Co^{2+} pathway should be significantly reduced when the HS−LS transition of Co^{2+} occurs, the resistance of $PbCoO_3$ exhibits an unusual increase with pressure up to 12.8 GPa. Above 15.2 GPa, however, the magnitude of resistance starts to decrease. More strikingly, the temperature dependence of resistance changes in nature. One finds that the resistance sharply increases by several orders of magnitude as the temperature decreases from 270 to 50 K at pressures below ∼15 GPa, whereas a weak temperature dependence with the change less than 1 order is found to occur once the pressure exceeds 15 GPa, although the insulating conductivity still shows up until 18.4 GPa, as characterized by the raising resistance on cooling (Figure 2a). These observations suggest that the spin state transition should complete around 15 GPa and other effects (such as Pb−Co charge transfer shown later) lead to the essential variation of resistivity in $PbCoO_3$ above this pressure.

Under further compression to 21.0 and 27.1 GPa, metallic electrical transport behavior occurs at higher temperatures as shown in Figure 2a and more clearly in Figure 2b, indicating the melting of the ordered LS-Co^{2+} and -Co^{3+} states near RT. Moreover, lowering the temperature changes the metallic state back to an insulating state, implying that the electronic states of Co^{2+} and/or Co^{3+} ions further change at lower temperatures. The critical temperature for the metal−insulator (MI) transition (T_{MI}) at 21.0 GPa is about 214 K. In general, higher pressures will reduce the T_{MI} and eventually realize the metallization at a wider temperature region. Unexpectedly, however, the T_{MI} of $PbCoO_3$ shifts toward higher temperatures with further compression. For example, the value of T_{MI} increases to 244 K at 27.1 GPa. Furthermore, in the whole temperature range we measured, the MI transition disappears and only the electrical insulating behavior is observed from 32.2 GPa up to 48.9 GPa, the maximum pressure we applied for electrical transport measurement as presented in Figure 2a. Therefore, if we plot the resistance values collected near RT as a function of pressure (Figure 2c), one can distinguish several different electrical characteristic features. Below about 15 GPa, the compound shows insulating behavior, and the resistance linearly increases due to the HS−LS transition of Co^{2+}. Above 15 GPa, there is an essential variation in electrical transport, and the resistance starts to decreases with pressure, indicating that a new mechanism rather than the spin state transition dominates the electrical transport, while the compound still maintains insulating behavior below ∼20 GPa. Between 20 and 30 GPa, the MI transition appears, and the T_{MI} unusually shifts toward higher temperature with further compression. Above 30 GPa, the reentrant insulating behavior is found to occur in the whole temperature region we measured, and the values of resistance linearly decrease with pressure up to 48.9 GPa due to the normal physical pressure effect. Note that during the pressure release, the electrical transitions are all reversible (see Supporting Information Figure S1).

To further understand the series of interesting variations observed in electrical transport measurements, we performed pressure dependent XES and XAS measurements at RT for characterizing the spin states and valence states of Co and Pb. Figure 3 shows the Co K_β emission spectra of $PbCoO_3$

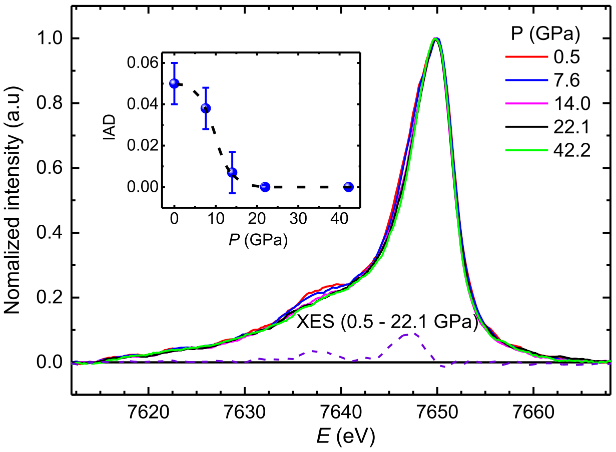

Figure 3. XES for Co K_β edge of $PbCoO_3$ at different pressures and room temperature. The pre-edge peak decreases with increasing pressure up to 22.1 GPa, indicating a HS to LS transition of Co^{2+}. The inset shows the pressure dependence of IAD, and the dash−dot curve is a guide for eyes.

measured at different pressures. At 0.5 GPa, the spectrum represents a main peak located at ∼7650 eV corresponding to the $K_{\beta1,3}$ line, and a pronounced satellite peak at ∼7637 eV corresponding to the $K_{\beta'}$ line. The intensity ratio of the low-energy $K_{\beta'}$ line to the main emission $K_{\beta1,3}$ line is proportional to the number of the unpaired electrons in the incomplete 3d shell[47,48] and can be used to determine the spin state of Co ion as a function of temperature[17,49] and/or pressure.[17,42,49−51] With increasing pressure, the intensity of the low-energy $K_{\beta'}$ line decreases and almost disappears above ∼15 GPa (Figure 3), suggesting a decreasing spin moment of Co^{2+} ion. The inset of Figure 3 contains a plot of the integrated absolute difference (IAD) as a function of pressure.[17,42,49−51] To get the IAD, all of the XES spectra were normalized with respect to the area under the curves and then shifted to have centers of mass at the same position. As an instance, the differential curve between 0.5 and 22.1 GPa is shown in Figure 3. In this situation, the IAD value presents a linear relationship with the average spin number. In $PbCoO_3$, the total IAD changes by about 0.043(10) in going from 0.5 to 22.1 GPa. In comparison, for a complete HS-Co^{3+} to LS-Co^{3+} transition with spin change $\Delta S = 2$, the IAD value is 0.15 as observed in $Sr_2Co_{0.5}Ir_{0.5}O_4$.[49] In the present $PbCoO_3$, when the HS Co^{2+} changes into the LS one, the average ΔS for the four Co ions per unit cell is 0.5, suggesting that the IAD value should be about 0.05. This value is comparable with the experimental observation, confirming the HS−LS transition of Co^{2+} in $PbCoO_3$. Since the IAD almost becomes zero with pressure going to about 15 GPa, we conclude that the spin state transition should complete around this pressure, in agreement with the electrical transport result. In addition, the continuous spin state transition was further supported by NPD under pressure as shown in Supporting Information Table S1 and Figure S2, where the observed shrinkage of Co^{2+}−O bond can be attributed to the HS to LS variation.

It is well-known that the XAS at the transition metal K edge is very sensitive to the valence state of transition metal.[52,53] This technique is generally used to identify the valence states of 3d transition metals. Figure 4a shows the Co K XAS spectra of $PbCoO_3$ measured at different pressures and normalized intensity $\mu = 0.8$.[50] At pressures below 15 GPa or above 30 GPa one can see a relatively weak linear higher-energy shift of the absorption edge with increasing pressure without changing line shape. Such shift was well studied in $RMnO_3$ as a physical pressure effect due to shortening Mn−O bond length under pressure.[54−56] On the other hand, there is an abrupt higher-energy shift from 20.2 to 29.3 GPa acompanying a variation of

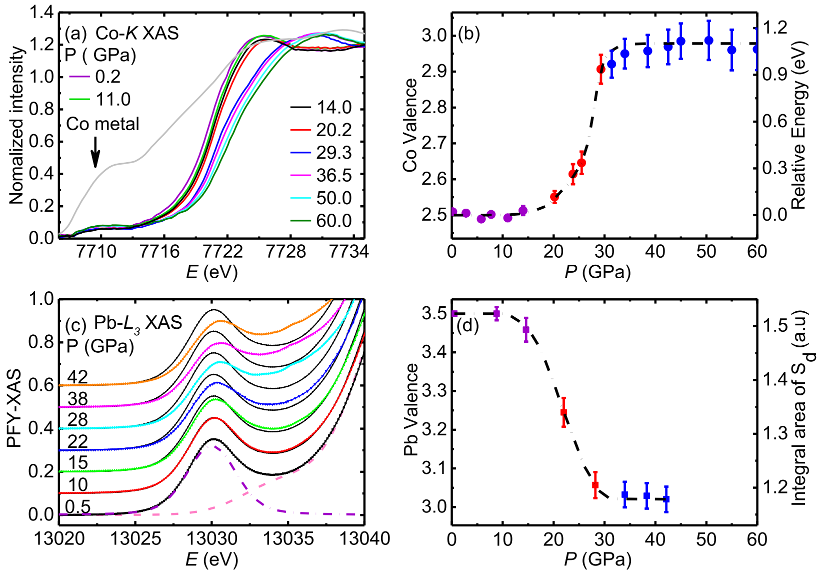

Figure 4. XAS of $PbCoO_3$ measured at different pressures and room temperature. (a) The Co K XAS spectra at some representative pressures. The XAS of Co metal as a reference at ambient pressure is also shown. (b) Relative energy shift of Co K edge as a function of pressure at the normalized intensity $\mu = 0.8$ after subtracting the background, and the valence state change of Co under pressure. The dot and dash curve is a guide for the eye. (c) Pre-edge peak S_d in the Pb L_3 XAS spectra measured using PFY mode at some representative pressures. For comparison, the XAS spectrum collected at 0.5 GPa is shown for the data taken at different pressures. The pink dash curve shows the background of PFY mode, and the purple dot and dash curve shows the pre-edge peak S_d after subtracting the background. (d) Integral area of S_d and the valence state change of Pb as a function of pressure. The dot and dash curve is a guide for eyes.

https://dx.doi.org/10.1021/jacs.9b13508
J. Am. Chem. Soc. 2020, 142, 5731−5741

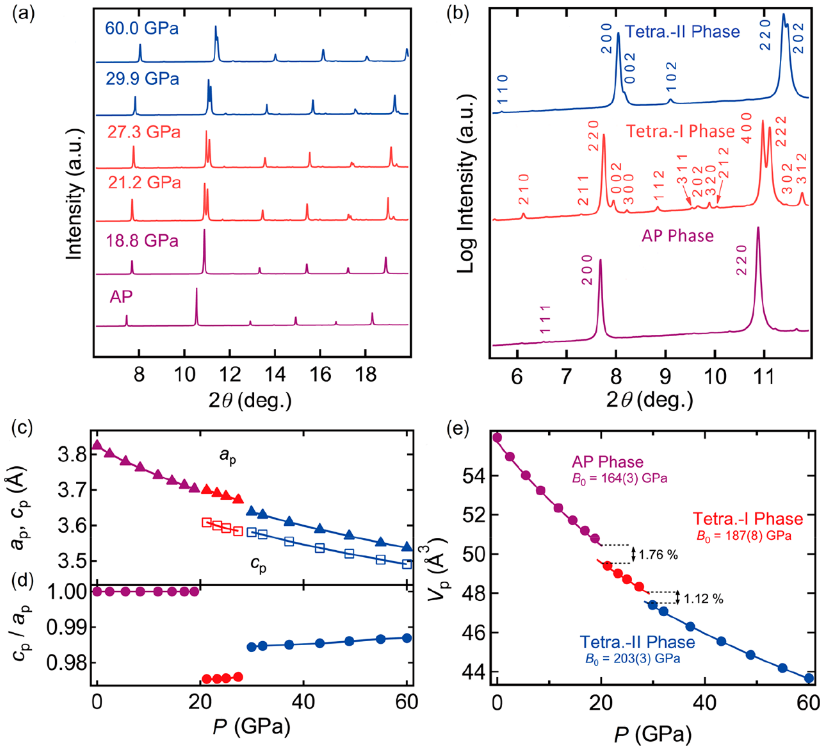

Figure 5. High-pressure SXRD patterns and related structural data. (a) Representative SXRD patterns collected at different pressures and room temperature. (b) SXRD patterns in log scale for the ambient pressure (AP) phase (P = 18.8 GPa), Tetra.-I phase (P = 27.3 GPa), and Tetra.-II phase (P = 60.0 GPa). The peaks of AP, Tetra.-I, and Tetra.-II phases are indexed with cubic $2a_p \times 2a_p \times 2a_p$, tetragonal $2\sqrt{2}a_p \times 2\sqrt{2}a_p \times 2a_p$, and tetragonal $2a_p \times 2a_p \times 2a_p$ unit cells, respectively. Pressure dependence of (c) normalized lattice parameters, (d) the ratio of a/c, and (e) unit cell volume. The curves in (e) show the fitting results based on the Birch−Murnaghan equation of state as described in the text.

spectral profile, indicating the changes of valence state and crystal structure as shown later. After subtraction of the physical pressure effect, the pressure dependent energy shift relative to 0.2 GPa as presented in Figure 4b (left scale) reflects a change of valence state of Co in $PbCoO_3$. One can see a considerable energy shift by about 1.1 ± 0.1 eV from 15 to 30 GPa. As a reference, when the valence changes from Co^{2+} to Co^{3+}, the energy shift is about 2.5 eV.[52] The observed Co K edge energy shift in $PbCoO_3$ suggests the average valence change by about 0.5 (i.e., from $Co^{2.5+}$ to $Co^{3.0+}$ in average), as illustrated in Figure 4b (right scale). To fulfill the charge balance requirement, one expects some Pb^{4+} changing to Pb^{2+} correspondingly.

Figure 4c presents the pressure dependent Pb L_3 XAS spectra of $PbCoO_3$. Unlike the XAS spectra at the transition metal L and K edges, where the energy positions of the strong white line and the absorption edge are very sensitive to the number of localized d valence electrons, at the Pb L edge there is no clear white line and energy position. Moreover, the Pb L absorption edge is strongly affected by crystal structure, so it is less sensitive to the Pb valence state. Therefore, it is not a trivial matter to determine the Pb valence state by using the chemical shift of the absorption edge. Fortunately, the Pb L_3 XAS spectrum taken from the high resolution partial fluorescence yield (PFY) mode provides an opportunity to identify the valence state of Pb. As shown in Figure 4c, one finds that there is a sharp lower energy shoulder S_d at 13,030 eV in the PFY spectrum. This lower energy pre-edge peak is assigned to the dipole allowed transition from the $2p^{3/2}$ core level to the unoccupied 6s states, while the main peak at 13 040 eV is assigned to the transitions from the $2p^{3/2}$ core level to the empty Pb 6d t_{2g} and e_g states, respectively.[57,58] It was found that the pre-edge peak S_d can be observed for Pb^{4+} ion with two 6s holes but is absent for Pb^{2+} ion with fully occupied 6s states. Thus, the spectral intensity of the pre-edge peak S_d represents the number of 6s holes and can be used to determine the valence change of Pb as a function of pressure. After subtracting the background (see the pink dashed curve in Figure 4c) originated from the edge jump and the Pb 5d states,[59] the spectral integral area of S_d as a function of pressure is presented in Figure 4d. The sharp reducing intensity with pressure going from 15 to 30 GPa indicates the valence decrease of Pb. Given the initial average valence state of $Pb^{3.5+}$ at lower pressure ($Pb^{2+}Pb^{4+}{}_3Co^{2+}{}_2Co^{3+}{}_2O_{12}$), the relative variation of the integral area of S_d suggests the change from $Pb^{3.5+}$ to $Pb^{3.0+}$. The Co K edge ($Co^{2.5+} \rightarrow Co^{3.0+}$) and Pb L edge ($Pb^{3.5+} \rightarrow Pb^{3.0+}$) XAS spectra thus confirm the Pb^{4+}−Co^{2+} intermetallic charge transfer which sets in around 15 GPa with a sharp change near 20 GPa and finishes at about 30 GPa. It should be noted that Ni K and Bi L_3 XAS was used to confirm the pressure induced intermetallic charge transfer transition in $BiNiO_3$ as well.[60]

To get deeper insight into the structural features during the spin state and metal−insulator transitions as well as the Pb−Co intermetallic charge transfer, high-pressure SXRD was carried out. Figure 5a shows the room-temperature SXRD patterns obtained at different pressures. With increasing pressure to 18.8 GPa, all the diffraction peaks systematically shift toward higher angle as expected from the volume contraction, and there is no visible trace for structural phase transition. Therefore, the A- and B-site ordered $Pn\bar{3}$ cubic crystal structure with a $2a_p \times 2a_p \times 2a_p$ supercell remains unchanged during the HS−LS transition of Co^{2+} (where a_p is the lattice parameter for a simple cubic ABO_3 perovskite). This can also account for the electrical insulating behavior observed below 20 GPa shown in Figure 2a. Once the room-temperature metallization takes place between 20 and 30 GPa (Figure 2c), a new high-pressure phase (Tetra.-I phase) appears in this pressure range. As shown in Figure 5a, the SXRD pattern collected at 21.2 GPa displays essentially a different profile from that measured at 18.8 GPa. For example, the single (220) peak around $2\theta = 10.8°$ in the cubic $Pn\overline{3}$ phase separates into two sharp diffraction peaks (400) and (222) in the Tetra.-I phase. Although the data can be indexed with a $2\sqrt{2}a_p \times 2\sqrt{2}a_p \times 2a_p$ tetragonal unit cell and possible space groups of $P4_2$ (No. 77), $P4_2/m$ (No. 84), or $P4_222$ (No. 93), we cannot determine the exact crystal structure (symmetry and atomic positions) for the new Tetra.-I phase because of the unreliable intensity ratio caused by the limited number of particles in a small space of the DAC. However, Le Bail fitting was conducted to understand the structural variations. As shown in Figure 5b, during the structural phase transition from the cubic $Pn\overline{3}$ to the Tetra.-I phase around 20 GPa, the normalized *a*-axis lattice constant expands whereas the *c*-axis shrinks. Moreover, the c/a ratio experiences a steep drop (Figure 5c). If the cell volume normalized to each formula unit is plotted as a function of pressure (Figure 5d), a considerable volume collapse is found to occur by about 1.76% at 20 GPa, implying that the structural transition is first-order in nature. The presence of coexisting two phases (cubic and Tetra.-I) at 19.7 GPa and 300 K supports the first-order transition (see Figure S3).

When the pressure further increases to 29.5 GPa at RT, a second crystal structure phase transition (Tetra.-II phase) takes place as presented in Figure 5a and Figure 5b. Le Bail analysis indicates another tetragonal lattice for this new phase with a $2a_p \times 2a_p \times 2a_p$ supercell with possible space groups of $P4_2mc$ (No. 105), P-$42c$ (No. 112), or $P4_2/mmc$ (No. 131). During the structural transition from the Tetra.-I to II phase, the normalized *a*-axis is reduced in a large degree while the *c*-axis expands slightly (Figure 5c). As a result, the c/a ratio increases remarkably. As seen from the relationship between pressure and the normalized cell volume in Figure 5d, the volume also experiences a discontinuous change from the Tetra.-I to II phase by about 1.12% at 30 GPa. The discontinuous decrease in the unit cell volume and the coexisting two phases (Tetra.-I and II) at 29.5 GPa indicate that the Tetra.-I to II phase transition is also first order (see Figure S3). Since charge transfer essentially changes the charge states and electronic configurations for two different metals, it usually leads to drastic magnetic and electrical variations as well as a sharp first-order structural phase transition, as reported in La/$BiCu_3Fe_4O_{12}$, $BiNiO_3$, and $PbCrO_3$.[28,29,38,61−64] The Tetra.-I to II transition of $PbCoO_3$ is also from the Pb^{4+}−Co^{2+} intermetallic charge transfer.

As shown in Figure 5e, the pressure dependence of cell volume for the three structural phases at RT can be well fitted by the isothermal Birch−Murnaghan equation of state with the function $P(V) = 1.5B_0[(V_0/V)^{7/3} - (V_0/V)^{5/3}] \times \{1 + 0.75(B_0' - 4)[(V_0/V)^{2/3} - 1]\}$, where the B_0 and B_0' are the bulk modulus and its pressure derivative, respectively.[65,66] In the case of $B_0' = 4$, which is a typical value for elastic lattices, the fitting gives $B_0 = 164(3)$ GPa for the cubic $Pn\overline{3}$ phase, 187(8) GPa for the Tetra.-I phase, and 203(3) GPa for the Tetra.-II phase. The value of B_0 in the cubic phase of $PbCoO_3$ is similar to that observed in the simple cubic perovskite $SrCoO_3$.[67]

As seen from the temperature dependent electrical measurements at different pressures (Figure 2), the high-pressure Tetra.-I phase is metallic whereas the Tetra.-II phase is insulating. Moreover, for the Tetra.-I phase occurring between about 20 and 30 GPa, lowering temperature triggers a metal-to-insulator transition. To understand the origin of this MI transition, low-temperature SXRD was performed at different pressures. As shown in Figure S4, at a pressure near 22 GPa, one finds that the insulating Tetra.-II phase emerges and coexists with the metallic Tetra.-I phase at temperatures below T_{MI} (e.g., at 150 and 100 K). As the pressure increases to about 27 GPa, these two tetragonal phases coexist at higher temperatures such as 200 K. These observations indicate that lowering the temperature favors the Pb^{4+}−Co^{2+} charge transfer as well as the formation of the insulating Tetra.-II phase, giving rise to the metal-to-insulator transition with unusual T_{MI} shift. One may notice that the phase boundary determined by SXRD study does not agree well with the M−I transition observed at 21 GPa and 214 K (see phase diagram shown later). It is most probably owing to the presence of temperature/pressure hysteresis at the first-order Tetra.-I to Tetra.-II transition as evidenced in the wide two phases coexisting region. The SXRD data points at 200 K were collected by pressure scan measurements at a constant temperature, while the resistivity measurements were conducted on heating at a constant pressure. Although the exact structural determination for both high-pressure phases remains for future resolution, the present pressure and temperature dependent SXRD results reveal significant structural variations accompanied by the pressure-induced metallization and the Pb−Co intermetallic charge transfer in $PbCoO_3$.

On the basis of the peculiar charge combination and crystal constitution, we now discuss the origin for the sensitive pressure dependence of the spin and charge states in $PbCoO_3$, as schematically shown in Figure 6. At ambient pressure, $PbCoO_3$ has a $Pb^{2+}Pb^{4+}{}_3Co^{2+}{}_2Co^{3+}{}_2O_{12}$ charge format as well as the A- and B-site ordered perovskite structure. Usually, a considerable charge difference (≥2) is needed between the B- and B′-site cations to form an ordered perovskite structure.[68] In the case of $PbCoO_3$, it is the large ionic size discrepancy between the HS Co^{2+} and LS Co^{3+} that stabilizes the rocksalt-

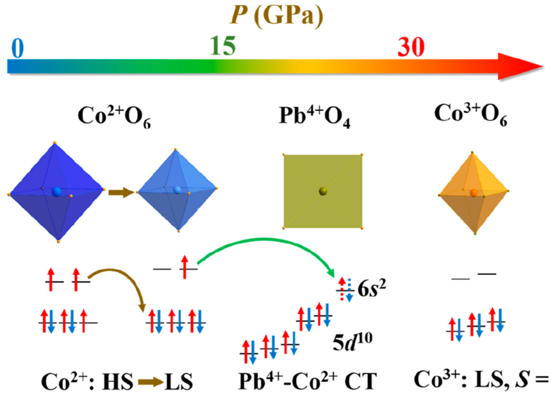

Figure 6. Shematic view of the origin of pressure induced spin state transition and charge transfer in $PbCoO_3$. The dot arrows in the $6s^2$ orbitals of Pb show the transferred electrons from the LS Co^{2+}. CT = charge transfer.

type ordered perovskite structure, although the charge difference is only 1. In most ABO_3 perovskites with the average B−O−B bond angle larger than 160°, the pressure induced volume shrinking is mainly attributed to the BO_6 octahedral titling and/or rotation in addition to the B−O bond length decrease. In the current $PbCoO_3$, however, the initial Co^{2+}−O−Co^{3+} bond angle has already decreased to about 140° to fill the small-size Pb^{4+} into the perovskite A-site. As a result, when the compound encounters external physical pressure, the $Co^{2+}O_6$ octahedra with significantly longer Co−O bond length than that of $Co^{3+}O_6$ have to reduce the volume by majorly decreasing the Co^{2+}−O distance (see Figure S2), giving rise to remarkable increase of $Co^{2+}O_6$ octahedral crystal field energy. Since the crystal field overcomes the Hund coupling energy, the high spin state of Co^{2+} changes to low spin. Therefore, a continuous HS−LS transition is found to occur in $PbCoO_3$ at pressure below 15 GPa, which is responsible for the unusual increase of resistance with pressure because the electronic density of state of $PbCoO_3$ near the Fermi surface is dominated by Co^{2+}.[37] In addition, first-principle calculations show that there exists visible hybridization between Pb^{4+} and Co^{2+} at ambient pressure, indicating that the empty 6s orbitals of Pb^{4+} have similar energy level as that of the e_g orbitals of Co^{2+}.[37] As mentioned above, high pressure increases the crystal field energy and induces the HS−LS transition of Co^{2+}. Correspondingly, the enhanced crystal field will also lift the energy level of the e_g orbitals. Thus, following the HS−LS transition, it is energetically favorable for electrons to transfer from the e_g orbitals of Co^{2+} to the 6s orbitals of Pb^{4+} under higher pressure, as we observed in experiment by the continuous Pb^{4+}−Co^{2+} intermetallic charge transfer between 15 and 30 GPa. Since the charge transfer decreases the component of Co^{2+} and therefore reduces the average ionic radius at this atomic site, the accumulated effect of charge transfer eventually breaks the B-site ordered perovskite structure to a disordered one, resulting in the first-order structure phase transition as well as the metallization with pressure up to 20 GPa near RT. Once the charge transfer completes at about 30 GPa, all the LS Co^{2+} changes to the LS Co^{3+} with $S = 0$. As a consequence, the compound displays another first-order structure transition and reenters an electrical insulating state. In addition to external pressure, lowering the temperature also favors the Pb^{4+}−Co^{2+} intermetallic charge transfer, leading to the coexistence of the insulating Tetra.-II phase and the metallic Tetra.-I between 20 and 30 GPa at lower temperatures.

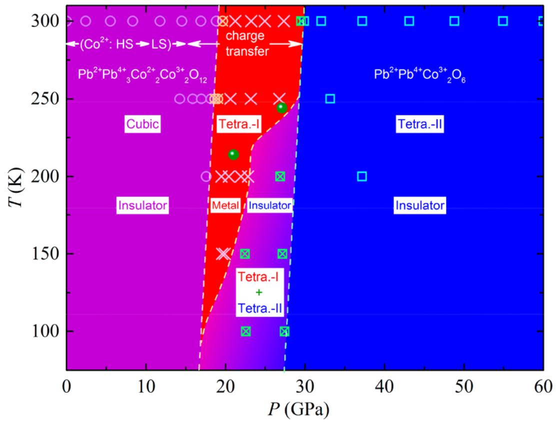

Figure 7. Pressure and temperature dependent phase diagram of $PbCoO_3$. The circle (○), cross (×), and square (□) respectively stand for the cubic, Tetra.-I, and Tetra.-II phases as determined from SXRD measurements. The dash curves approximately show the phase boundaries.

4. CONCLUSIONS

According to the high-pressure resistance, XES, XAS, and SXRD results described above, we obtain an interesting pressure and temperature dependent phase diagram for $PbCoO_3$ as shown in Figure 7. (i) Below ∼20 GPa, the compound maintains the A- and B-site ordered quadruple perovskite structure in the cubic $Pn\bar{3}$ symmetry with the charge combination of $Pb^{2+}Pb^{4+}{}_3Co^{2+}{}_2Co^{3+}{}_2O_{12}$ ($Pb^{3.5+}Co^{2.5+}O_3$ in average). However, the HS state of Co^{2+} sensitively depends on external pressure. It sluggishly changes to a LS state with increasing pressure up to about 15 GPa. When the spin state transition finishes, pressure induced intermetallic charge transfer starts to occur between Co^{2+} and Pb^{4+} ions, leading to essentially different electrical transport properties at pressures below and above 15 GPa. (ii) Between approximately 20 and 30 GPa, metallization is observed due to the accumulated effect of Pb^{4+}-Co^{2+} charge transfer near RT, strongly suggesting the melting of the ordered low-spin Co^{2+} and Co^{3+} states into a mixed $Co^{2.5+}$ on average. This is consistent with the first-order structural phase transition to the Tetra.-I phase. The Pb^{4+}−Co^{2+} charge transfer still takes place in the Tetra.-I phase, making the LS-Co^{2+} state be oxidized to the LS-Co^{3+} one. Since the composition of the strongly insulating LS-Co^{3+} is enhanced by the charge transfer, the T_{MI} of $PbCoO_3$ exhibits an unusual shift toward higher temperatures on compression. Moreover, at fixed pressure in this phase, lowering temperature favors the Pb^{4+}-Co^{2+} ICT as well as the formation of the insulating Tetra.-II phase, which is responsible for the observed low-temperature MI transition. (iii) With pressure up to ∼30 GPa at RT, the Pb−Co intermetallic charge transfer completes, changing the charge combination to be $Pb^{3.0+}Co^{3.0+}O_3$ on average. Accordingly, the compound experiences another first-order structure phase transition toward the Tetra.-II phase with considerable volume shrinking. In the Tetra.-II phase, all the transition-metal sites are occupied by the LS-Co^{3+} with $S = 0$. Therefore, electrical insulating behavior shows again in the whole temperature region we measured. The present $PbCoO_3$ provides the first example where spin state, charge state, crystal structure, and metal−insulator transitions take place collectively in the same material system, opening up a new avenue for studying sequential spin state transition and intermetallic charge transfer as well as related multifunctional transformations.

■ ASSOCIATED CONTENT

Supporting Information

The Supporting Information is available free of charge at https://pubs.acs.org/doi/10.1021/jacs.9b13508.

Refined structural parameters for $PbCoO_3$ at 290 K under various pressures based on the neutron powder diffraction; electrical transport properties of $PbCoO_3$ during pressure release from 48.9 to 1.6 GPa; pressure dependence of the average bond lengths calculated from the structural parameters determined by Rietveld analysis of neutron diffraction data; synchrotron X-ray diffraction (SXRD) patterns measured at different pressures and temperatures (PDF)

AUTHOR INFORMATION

Corresponding Authors

Jinming Chen − *National Synchrotron Radiation Research Center, Hsinchu 30076, Taiwan, R.O.C.*; Email: jmchen@nsrrc.org.tw

Masaki Azuma − *Laboratory for Materials and Structures, Tokyo Institute of Technology, Yokohama 226-8503, Japan; Kanagawa Institute of Industrial Science and Technology, Ebina 243-0435, Japan;* orcid.org/0000-0002-8378-321X; Email: mazuma@msl.titech.ac.jp

Youwen Long − *Beijing National Laboratory for Condensed Matter Physics, Institute of Physics, Chinese Academy of Sciences, Beijing 100190, China; School of Physics, University of Chinese Academy of Sciences, Beijing 100049, China; Songshan Lake Materials Laboratory, Dongguan, Guangdong 523808, China;* orcid.org/0000-0002-8587-7818; Email: ywlong@iphy.ac.cn

Authors

Zhehong Liu − *Beijing National Laboratory for Condensed Matter Physics, Institute of Physics, Chinese Academy of Sciences, Beijing 100190, China; School of Physics, University of Chinese Academy of Sciences, Beijing 100049, China*

Yuki Sakai − *Kanagawa Institute of Industrial Science and Technology, Ebina 243-0435, Japan; Laboratory for Materials and Structures, Tokyo Institute of Technology, Yokohama 226-8503, Japan*

Junye Yang − *Beijing National Laboratory for Condensed Matter Physics, Institute of Physics, Chinese Academy of Sciences, Beijing 100190, China*

Wenmin Li − *Beijing National Laboratory for Condensed Matter Physics, Institute of Physics, Chinese Academy of Sciences, Beijing 100190, China; School of Physics, University of Chinese Academy of Sciences, Beijing 100049, China*

Ying Liu − *Beijing National Laboratory for Condensed Matter Physics, Institute of Physics, Chinese Academy of Sciences, Beijing 100190, China; School of Physics, University of Chinese Academy of Sciences, Beijing 100049, China*

Xubin Ye − *Beijing National Laboratory for Condensed Matter Physics, Institute of Physics, Chinese Academy of Sciences, Beijing 100190, China; School of Physics, University of Chinese Academy of Sciences, Beijing 100049, China*

Shijun Qin − *Beijing National Laboratory for Condensed Matter Physics, Institute of Physics, Chinese Academy of Sciences, Beijing 100190, China; School of Physics, University of Chinese Academy of Sciences, Beijing 100049, China*

Stefano Agrestini − *Max-Planck Institute for Chemical Physics of Solids, 01187 Dresden, Germany*

Kai Chen − *Max-Planck Institute for Chemical Physics of Solids, 01187 Dresden, Germany;* orcid.org/0000-0002-7667-3063

Sheng-Chieh Liao − *Max-Planck Institute for Chemical Physics of Solids, 01187 Dresden, Germany*

Shu-Chih Haw − *National Synchrotron Radiation Research Center, Hsinchu 30076, Taiwan, R.O.C.*

Francois Baudelet − *Synchrotron SOLEIL, 91192 GIF-sur-Yvette, France*

Hirofumi Ishii − *National Synchrotron Radiation Research Center, Hsinchu 30076, Taiwan, R.O.C.*

Takumi Nishikubo − *Laboratory for Materials and Structures, Tokyo Institute of Technology, Yokohama 226-8503, Japan*

Hayato Ishizaki − *Laboratory for Materials and Structures, Tokyo Institute of Technology, Yokohama 226-8503, Japan*

Tatsuru Yamamoto − *Laboratory for Materials and Structures, Tokyo Institute of Technology, Yokohama 226-8503, Japan*

Zhao Pan − *Laboratory for Materials and Structures, Tokyo Institute of Technology, Yokohama 226-8503, Japan;* orcid.org/0000-0002-8693-2508

Masayuki Fukuda − *Laboratory for Materials and Structures, Tokyo Institute of Technology, Yokohama 226-8503, Japan*

Kotaro Ohashi − *Laboratory for Materials and Structures, Tokyo Institute of Technology, Yokohama 226-8503, Japan*

Kana Matsuno − *Laboratory for Materials and Structures, Tokyo Institute of Technology, Yokohama 226-8503, Japan*

Akihiko Machida − *Quantum Beam Science Research Directorate, National Institutes for Quantum and Radiological Science and Technology, Sayo, Hyogo 679-5148, Japan*

Tetsu Watanuki − *Quantum Beam Science Research Directorate, National Institutes for Quantum and Radiological Science and Technology, Sayo, Hyogo 679-5148, Japan*

Saori I. Kawaguchi − *Japan Synchrotron Radiation Research Institute, Sayo, Hyogo 679-5198, Japan*

Angel M. Arevalo-Lopez − *Centre for Science at Extreme Conditions and School of Chemistry, University of Edinburgh, Edinburgh EH9 3JZ, United Kingdom*

Changqing Jin − *Beijing National Laboratory for Condensed Matter Physics, Institute of Physics, Chinese Academy of Sciences, Beijing 100190, China; School of Physics, University of Chinese Academy of Sciences, Beijing 100049, China*

Zhiwei Hu − *Max-Planck Institute for Chemical Physics of Solids, 01187 Dresden, Germany*

J. Paul Attfield − *Centre for Science at Extreme Conditions and School of Chemistry, University of Edinburgh, Edinburgh EH9 3JZ, United Kingdom;* orcid.org/0000-0001-9763-3987

Complete contact information is available at:
https://pubs.acs.org/10.1021/jacs.9b13508

Notes

The authors declare no competing financial interest.

ACKNOWLEDGMENTS

The authors thank Y. F. Yang and Y. Y. Cao for fruitful discussions. This work was supported by the National Key R&D Program of China (Grants 2018YFE0103200 and 2018YFA0305700), the National Natural Science Foundation of China (Grants 11934017, 51772324, 11921004, and 11574378), the Chinese Academy of Sciences (Grants QYZDB-SSW-SLH013, GJHZ1773, YZ201555), the Ministry of Science and Technology (Grant MOST 105-2113-M-213-005-MY3), JSPS KAKENHI Grants JP18H05208 and JP19H05625 from the Japan Society for the Promotion of Science (JSPS) and JSPS and CAS under the Japan-China Scientific Cooperation Program. Y.L. was partially supported by World Research Hub Initiative, Institute of Innovative Research, Tokyo Institute of Technology and Collaborative Research Projects, Laboratory for Materials and Structures, Tokyo Institute of Technology. The synchrotron-radiation X-ray diffraction experiments were performed using a QST experimental station at JAEA beamline BL22XU, SPring-8, with the approval of the Japan Synchrotron Radiation Research Institute (Proposals 2016A3784, 2017A3781, 2017B3751, 2018A3782, 2019A3781, and 2019B3781), and were supported by QST Advanced Characterization Nanotechnology Platform under the remit of "Nanotechnology Platform" of the Ministry of Education, Culture, Sports, Science and Technology, Japan (Proposals A-16-QS-0011, A-17-QS-0010, A-18-QS-0014, A-19-QS-0015, and A-19-QS-0039).

REFERENCES

(1) Keimer, B.; Kivelson, S. A.; Norman, M. R.; Uchida, S.; Zaanen, J. From quantum matter to high-temperature superconductivity in copper oxides. *Nature* **2015**, *518*, 179−186.

(2) Imada, M.; Fujimori, A.; Tokura, Y. Metal-insulator transitions. *Rev. Mod. Phys.* **1998**, *70*, 1039−1263.

(3) Dagotto, E.; Hotta, T.; Moreo, A. Colossal magnetoresistant materials: the key role of phase separation. *Phys. Rep.* **2001**, *344*, 1−153.

(4) Salamon, M. B.; Jaime, M. The physics of manganites: structure and transport. *Rev. Mod. Phys.* **2001**, *73*, 583−628.

(5) Hemberger, J.; Lobina, S.; Krug von Nidda, H.-A.; Tristan, N.; Ivanov, V. Y.; Mukhin, A. A.; Balbashov, A. M.; Loidl, A. Complex interplay of 3d and 4f magnetism in La$_{1-x}$Gd$_x$MnO$_3$. *Phys. Rev. B: Condens. Matter Mater. Phys.* **2004**, *70*, No. 024414.

(6) Seo, J. S.; Whang, D.; Lee, H.; Jun, S. I.; Oh, J.; Jeon, Y. J.; Kim, K. A homochiral metal−organic porous material for enantioselective separation and catalysis. *Nature* **2000**, *404*, 982−986.

(7) Tokura, Y.; Seki, S.; Nagaosa, N. Multiferroics of spin origin. *Rep. Prog. Phys.* **2014**, *77*, No. 076501.

(8) Wang, X.; Chai, Y. S.; Zhou, L.; Cao, H. B.; Cruz, C.-D.; Yang, J. Y.; Dai, J. H.; Yin, Y. Y.; Yuan, Z.; Zhang, S.; Yu, R. Z.; Azuma, M.; Shimakawa, Y.; Zhang, H. M.; Dong, S.; Sun, Y.; Jin, C. Q.; Long, Y. W. Observation of Magnetoelectric Multiferroicity in a Cubic Perovskite System: LaMn$_3$Cr$_4$O$_{12}$. *Phys. Rev. Lett.* **2015**, *115*, No. 087601.

(9) Zhou, L.; Dai, J. H.; Chai, Y. S.; Zhang, H. M.; Dong, S.; Cao, H. B.; Calder, S.; Yin, Y. Y.; Wang, X.; Shen, X. D.; Liu, Z. H.; Saito, T.; Shimakawa, Y.; Hojo, H.; Ikuhara, Y.; Azuma, M.; Hu, Z. W.; Sun, Y.; Jin, C. Q.; Long, Y. W. Realization of Large Electric Polarization and Strong Magnetoelectric Coupling in BiMn$_3$Cr$_4$O$_{12}$. *Adv. Mater.* **2017**, *29*, 1703435.

(10) Haverkort, M. W.; Hu, Z.; Cezar, J. C.; Burnus, T.; Hartmann, H.; Reuther, M.; Zobel, C.; Lorenz, T.; Tanaka, A.; Brookes, N. B.; Hsieh, H. H.; Lin, H.-J.; Chen, C. T.; Tjeng, L. H. Spin State Transition in Studied Using Soft X-ray Absorption Spectroscopy and Magnetic Circular Dichroism. *Phys. Rev. Lett.* **2006**, *97*, 176405.

(11) Zobel, C.; Kriener, M.; Bruns, D.; Baier, J.; Grüninger, M.; Lorenz, T.; Reutler, P.; Revcolevschi, A. Evidence for a low-spin to intermediate-spin state transition in LaCoO$_3$. *Phys. Rev. B: Condens. Matter Mater. Phys.* **2005**, *71*, No. 019902.

(12) Křápek, V.; Novák, P.; Kuneš, J.; Novoselov, D.; Korotin, D. M.; Anisimov, V. I. Spin state transition and covalent bonding in LaCoO$_3$. *Phys. Rev. B: Condens. Matter Mater. Phys.* **2012**, *86*, 195104.

(13) Altarawneh, M. M.; Chern, G.-W.; Harrison, N.; Batista, C. D.; Uchida, A.; Jaime, M.; Rickel, D. G.; Crooker, S. A.; Mielke, C. H.; Betts, J. B.; Mitchell, J. F.; Hoch, M. J. R. Cascade of Magnetic Field Induced Spin Transitions in LaCoO$_3$. *Phys. Rev. Lett.* **2012**, *109*, No. 037201.

(14) Ikeda, A.; Nomura, T.; Matsuda, Y. H.; Matsuo, A.; Kindo, K.; Sato, K. Spin state ordering of strongly correlating LaCoO$_3$ induced at ultrahigh magnetic fields. *Phys. Rev. B: Condens. Matter Mater. Phys.* **2016**, *93*, No. 220401(R).

(15) Chakrabarti, B.; Birol, T.; Haule, K. Role of entropy and structural parameters in the spin-state transition of LaCoO$_3$. *Phys. Rev. Materials* **2017**, *1*, No. 064403.

(16) Klie, R. F.; Zheng, J. C.; Zhu, Y.; Varela, M.; Wu, J.; Leighton, C. Direct Measurement of the Low-Temperature Spin-State Transition in LaCoO$_3$. *Phys. Rev. Lett.* **2007**, *99*, No. 047203.

(17) Vankó, G.; Rueff, J. P.; Mattila, A.; Németh, Z.; Shukla, A. Temperature- and pressure-induced spin-state transitions in LaCoO3. *Phys. Rev. B: Condens. Matter Mater. Phys.* **2006**, *73*, No. 024424.

(18) Mattila, A.; Rueff, J.-P.; Badro, J.; Vankó, G.; Shukla, A. Metal-ligand interplay in strongly correlated oxides: A parametrized phase diagram for pressure-induced spin transitions. *Phys. Rev. Lett.* **2007**, *98*, 196404.

(19) Lengsdorf, R.; Rueff, J.-P.; Vankó, G.; Lorenz, T.; Tjeng, L. H.; Abd-Elmeguid, M. M. Spin-state-driven metal-insulator transition in (La,Sr)CoO$_3$ under high-pressure. *Phys. Rev. B: Condens. Matter Mater. Phys.* **2007**, *75*, No. 180401(R).

(20) Kim, B.; Kim, K.; Min, B. I. Universal metastability of the low-spin state in Co^{2+} systems: Non-Mott type pressure-induced spin-state transition in CoCl$_2$. *Phys. Rev. B: Condens. Matter Mater. Phys.* **2014**, *89*, 115131.

(21) Ding, Y.; Fernandez-Rodriguez, J.; Kim, J.; Li, F. F.; Casa, D.; Upton, M.; Gog, T.; Mao, H.-K.; van Veenendaal, M. Spin-ordering mediated orbital hybridization in CoO at high pressures. *Phys. Rev. B: Condens. Matter Mater. Phys.* **2012**, *86*, No. 094107.

(22) Leonov, I.; Ponomareva, A. V.; Nazarov, R.; Abrikosov, I. A. Pressure-induced spin-state transition of iron in magnesiowüstite (Fe,Mg)O. *Phys. Rev. B: Condens. Matter Mater. Phys.* **2017**, *96*, No. 075136.

(23) Lin, J.-F.; Gavriliuk, A. G.; Struzhkin, V. V.; Jacobsen, S. D.; Sturhahn, W.; Hu, M. Y.; Chow, P.; Yoo, C.-S. Pressure-induced electronic spin transition of iron in magnesiowustite-(Mg,Fe)O. *Phys. Rev. B: Condens. Matter Mater. Phys.* **2006**, *73*, 113107.

(24) Javaid, S.; Akhtar, M. J.; Ahmad, I.; Younas, M.; Shah, S. H.; Ahmad, I. Pressure driven spin crossover and isostructural phase transition in LaFeO$_3$. *J. Appl. Phys.* **2013**, *114*, 243712.

(25) Takano, M.; Nasu, S.; Abe, T.; Yamamoto, K.; Endo, S.; Takeda, Y.; Goodenough, J. B. Pressure-induced high-spin to low-spin transition in CaFeO$_3$. *Phys. Rev. Lett.* **1991**, *67*, 3267−3270.

(26) Kuneš, J.; Lukoyanov, A. V.; Anisimov, V. I.; Scalettar, R. T.; Pickett, W. E. Collapse of magnetic moment drives the Mott transition in MnO. *Nat. Mater.* **2008**, *7*, 198−202.

(27) Long, Y. W.; Hayashi, N.; Saito, T.; Azuma, M.; Muranaka, S.; Shimakawa, Y. Temperature-induced A−B intersite charge transfer in an A-site-ordered LaCu$_3$Fe$_4$O$_{12}$ perovskite. *Nature* **2009**, *458*, 60−63.

(28) Long, Y. W.; Kawakami, T.; Chen, W. T.; Saito, T.; Watanuki, T.; Nakakura, Y.; Liu, Q. Q.; Jin, C. Q.; Shimakawa, Y. Pressure Effect on Intersite Charge Transfer in A-site-Ordered Double-Perovskite-Structure Oxide. *Chem. Mater.* **2012**, *24*, 2235−2239.

(29) Azuma, M.; Carlsson, S.; Rodgers, J.; Tucker, M. G.; Tsujimoto, M.; Ishiwata, S.; Isoda, S.; Shimakawa, Y.; Takano, M.; Attfield, J. P. Pressure-Induced Intermetallic Valence Transition in BiNiO3. *J. Am. Chem. Soc.* **2007**, *129*, 14433−14436.

(30) Guillou, F.; Kummer, K.; Bréard, Y.; Hervé, L.; Hardy, V. Valence and spin-state transition in cobaltates revisited by x-ray magnetic circular dichroism. *Phys. Rev. B: Condens. Matter Mater. Phys.* **2017**, *95*, 174445.

(31) Hejtmánek, J.; Šantavá, E.; Knížek, K.; Maryško, M.; Jirák, Z.; Naito, T.; Sasaki, H.; Fujishiro, H. Metal-insulator transition and the Pr^{3+}/Pr^{4+} valence shift in (Pr$_{1-y}$Y$_y$)$_{0.7}$Ca$_{0.3}$CoO$_3$. *Phys. Rev. B: Condens. Matter Mater. Phys.* **2010**, *82*, 165107.

(32) Guillou, F.; Zhang, Q.; Hu, Z.; Kuo, C. Y.; Chin, Y. Y.; Lin, H. J.; Chen, C. T.; Tanaka, A.; Tjeng, L. H.; Hardy, V. Coupled valence and spin state transition in (Pr$_{0.7}$Sm$_{0.3}$)$_{0.7}$Ca$_{0.3}$CoO$_3$. *Phys. Rev. B: Condens. Matter Mater. Phys.* **2013**, *87*, 115114.

(33) Chen, J. M.; Lee, J. M.; Haw, S. C.; Chen, S. A.; Hardy, V.; Guillou, F.; Chen, S. W.; Kuo, C. Y.; Pao, C. W.; Lee, J. F.; Hiraoka, N.; Ishii, H.; Tsuei, K. D.; Hu, Z. Evolution of spin and valence states of (Pr$_{0.7}$Sm$_{0.3}$)$_{0.7}$Ca$_{0.3}$CoO$_3$ at high temperature and high pressure. *Phys. Rev. B: Condens. Matter Mater. Phys.* **2014**, *90*, No. 035107.

(34) García-Munoz, G. L.; Frontera, G.; Baron-Gonzalez, A. J.; Valencia, S.; Blasco, J.; Feyerherm, R.; Dudzik, E.; Abrudan, R.; Radu, F. Valence transition in (Pr,Ca)CoO$_3$ cobaltites: Charge migration at the metal-insulator transition. *Phys. Rev. B: Condens. Matter Mater. Phys.* **2011**, *84*, No. 045104.

(35) Hejtmanek, J.; Jirak, Z.; Kaman, O.; Knizek, K.; Santava, E.; Nitta, K.; Naito, T.; Fujishiro, H. Phase transition in Pr$_{0.5}$Ca$_{0.5}$CoO$_3$ and related cobaltites. *Eur. Phys. J. B* **2013**, *86*, 305.

(36) Fujita, T.; Miyashita, T.; Yasui, Y.; Kobayashi, Y.; Sato, M.; Nishibori, E.; Sakata, M.; Shimojo, Y.; Igawa, N.; Ishii, Y.; Kakurai, K.; Adachi, T.; Ohishi, Y.; Takata, M. Transport and Magnetic Studies on

the Spin State Transition of $Pr_{1-x}Ca_xCoO_3$ up to High Pressure. *J. Phys. Soc. Jpn.* **2004**, *73*, 1987−1997.

(37) Sakai, Y.; Yang, J. Y.; Yu, R. Z.; Hojo, H.; Yamada, I.; Miao, P.; Lee, S.; Torii, S.; Kamiyama, T.; Ležaić, M.; Bihlmayer, G.; Mizumaki, M.; Komiyama, J.; Mizokawa, T.; Yamamoto, H.; Nishikubo, T.; Hattori, Y.; Oka, K.; Yin, Y. Y.; Dai, J. H.; Li, W. M.; Ueda, S.; Aimi, A.; Mori, D.; Inaguma, Y.; Hu, Z. W.; Uozumi, T.; Jin, C. Q.; Long, Y. W.; Azuma, M. A-Site and B-Site Charge Orderings in an s−d Level Controlled Perovskite Oxide $PbCoO_3$. *J. Am. Chem. Soc.* **2017**, *139*, 4574−4581.

(38) Huang, L. Y.; Wang, L.; Dai, X. Pressure-driven orbital selective insulator-to-metal transition and spin-state crossover in cubic CoO. *Phys. Rev. B: Condens. Matter Mater. Phys.* **2012**, *85*, 245110.

(39) Lou, F.; Luo, W.; Feng, J.; Xiang, H. Genetic algorithm prediction of pressure-induced multiferroicity in the perovskite $PbCoO_3$. *Phys. Rev. B: Condens. Matter Mater. Phys.* **2019**, *99*, 205104.

(40) Zhang, J. L.; Zhang, S. J.; Weng, H. M.; Zhang, W.; Yang, L. X.; Liu, Q. Q.; Feng, S. M.; Wang, X. C.; Yu, R. C.; Cao, L. Z.; Wang, L.; Yang, W. G.; Liu, H. Z.; Zhao, W. Y.; Zhang, S. C.; Dai, X.; Fang, Z.; Jin, C. Q. Pressure-induced superconductivity in topological parent compound Bi_2Te_3. *Proc. Natl. Acad. Sci. U. S. A.* **2011**, *108*, 24−28.

(41) Mao, H. K.; Xu, J.; Bell, P. M. Calibration of the ruby pressure gauge to 800 kbar under quasi-hydrostatic conditions. *J. Geophys. Res.* **1986**, *91*, 4673−4676.

(42) Chen, J. M.; Chin, Y. Y.; Valldor, M.; Hu, Z. W.; Lee, J. M.; Haw, S. C.; Hiraoka, N.; Ishii, H.; Pao, C. W.; Tsuei, K. D.; Lee, J. F.; Lin, H. J.; Jang, L. Y.; Tanaka, A.; Chen, C. T.; Tjeng, L. H. A Complete High-to-Low spin state Transition of Trivalent Cobalt Ion in Octahedral Symmetry in $SrCo_{0.5}Ru_{0.5}O_{3-\delta}$. *J. Am. Chem. Soc.* **2014**, *136* (4), 1514−1519.

(43) Izumi, F.; Momma, K. Three-dimensional visualization in powder diffraction. *Solid State Phenom.* **2007**, *130*, 15−20.

(44) Besson, J. M.; Nelmes, R. J.; Hamel, G.; Loveday, J. S.; Weill, G.; Hull, S. Neutron powder diffraction above 10 GPa. *Phys. B* **1992**, *180*, 907−910.

(45) Larson, A. C.; Dreele, V.; General, R. B. Structural Analysis System (GSAS). Los Alamos National Laboratory Report; Los Almos National Laboratory: Los Alamos, NM, 2000; pp 86−748.

(46) Chang, C. F.; Hu, Z.; Wu, H.; Burnus, T.; Hollmann, N.; Benomar, M.; Lorenz, T.; Tanaka, A.; Lin, H.-J.; Hsieh, H. H.; Chen, C. T.; Tjeng, L. H. Spin Blockade, Orbital Occupation, and Charge Ordering in $La_{1.5}Sr_{0.5}CoO_4$. *Phys. Rev. Lett.* **2009**, *102*, 116401.

(47) Tsutsumi, K.; Nakamori, H.; Ichikawa, K. X-ray Mn K_β emission spectra of manganese oxides and manganates. *Phys. Rev. B* **1976**, *13*, 929−933.

(48) Vankó, G.; Neisius, T.; Molnár, G.; Renz, F.; Kárpáti, S.; Shukla, A.; de Groot, F. M. F. Probing the 3d Spin Momentum with X-ray Emission Spectroscopy: The Case of Molecular-Spin Transitions. *J. Phys. Chem. B* **2006**, *110*, 11647−11653.

(49) Chin, Y. Y.; Lin, H. J.; Hu, Z. W.; Kuo, C. Y.; Mikhailova, D.; Lee, J. M.; Haw, S. C.; Chen, S. A.; Schnelle, W.; Ishii, H.; Hiraoka, N.; Liao, Y. Y.; Tsuei, K. D.; Tanaka, A.; Tjeng, L. H.; Chen, C. T.; Chen, J. M. Relation between the Co-O bond lengths and the spin state of Co in layered cobaltates: a high-pressure study. *Sci. Rep.* **2017**, *7*, 3656.

(50) Chen, J. M.; Lee, J. M.; Haw, S. C.; Chen, S. A.; Hardy, V.; Guillou, F.; Chen, S. W.; Kuo, C. Y.; Pao, C. W.; Lee, J. F.; Hiraoka, N.; Ishii, H.; Tsuei, K. D.; Hu, Z. Evolution of spin and valence states of $(Pr_{0.7}Sm_{0.3})_{0.7}Ca_{0.3}CoO_3$ at high temperature and high pressure. *Phys. Rev. B: Condens. Matter Mater. Phys.* **2014**, *90*, No. 035107.

(51) Oka, K.; Azuma, M.; Chen, W. T.; Yusa, H.; Belik, A. A.; Takayama-Muromachi, E.; Mizumaki, M.; Ishimatsu, N.; Hiraoka, N.; Tsujimoto, M.; Tucker, M. G.; Attfield, J. P.; Shimakawa, Y. Pressure-Induced Spin-State Transition in $BiCoO_3$. *J. Am. Chem. Soc.* **2010**, *132* (27), 9438−9443.

(52) Yang, J. Y.; Zhou, L.; Cheng, J. G.; Hu, Z. W.; Kuo, C. Y.; Pao, C. W.; Jang, L. Y.; Lee, J. Y.; Dai, J. H.; Zhang, S. J.; Feng, S. M.; Kong, P. P.; Yuan, Z.; Yuan, J.; Uwatoko, Y.; Liu, T.; Jin, C. Q.; Long, Y. W. Charge Transfer Induced Multifunctional Transitions with Sensitive Pressure Manipulation in a Metal−Organic Framework. *Inorg. Chem.* **2015**, *54* (13), 6433−6438.

(53) Croft, M.; Sills, D.; Greenblatt, M.; Lee, C.; Cheong, S.-W.; Ramanujachary, K. V.; Tran, D. Systematic Mn d-configuration change in the $La_{1-x}Ca_xMnO_3$ system: A Mn K-edge XAS study. *Phys. Rev. B: Condens. Matter Mater. Phys.* **1997**, *55*, 8726−8732.

(54) Ramos, A. Y.; Souza-Neto, N. M.; Tolentino, H. C. N.; Bunau, O.; Joly, Y.; Grenier, S.; Itié, J.-P.; Flank, A.-M.; Lagarde, P.; Caneiro, A. Bandwidth-driven nature of the pressure-induced metal state of $LaMnO_3$. *EPL* **2011**, *96*, 36002.

(55) Chen, J. M.; Chou, T. L.; Lee, J. M.; Chen, S. A.; Chan, T. S.; Chen, T. H.; Lu, K. T.; Chuang, W. T.; Sheu, H.-S.; Chen, S. W.; Lin, C. M.; Hiraoka, N.; Ishii, H.; Tsuei, K. D.; Yang, T. J. Pressure-induced structural distortion of $TbMnO_3$: A combined x-ray diffraction and x-ray absorption spectroscopy study. *Phys. Rev. B: Condens. Matter Mater. Phys.* **2009**, *79*, 165110.

(56) Chen, J. M.; Lee, J. M.; Chou, T. L.; Chen, S. A.; Huang, S. W.; Jeng, H. T.; Lu, K. T.; Chen, T. H.; Liang, Y. C.; Chen, S. W.; Chuang, W. T.; Sheu, H.-S.; Hiraoka, N.; Ishii, H.; Tsuei, K. D.; Huang, E.; Lin, C. M.; Yang, T. J. Pressure-dependent electronic structures in multiferroic: A combined lifetime broadening-suppressed x-ray absorption spectroscopy and ab initio electronic structure study. *J. Chem. Phys.* **2010**, *133*, 154510.

(57) Liang, G.; Liu, R. S.; Wang, L. V. XANES study of the valence of Pb in $(Tl_{0.5}Pb_{0.5})Sr_2Ca_{1-x}Y_xCu_2O_{7-\delta}$. *Int. J. Mod. Phys. B* **1999**, *13*, 3693−3696.

(58) Chen, K.; Mijiti, Y.; Agrestini, S.; Liao, S. C.; Li, X.; Zhou, J. S.; Di Cicco, A.; Baudelet, F.; Tjeng, L. H.; Hu, Z. Valence State of Pb in Transition Metal Perovskites $PbTMO_3$ (TM = Ti, Ni) Determined From X-Ray Absorption Near-Edge Spectroscopy. *Phys. Status Solidi B* **2018**, *255*, 1800014.

(59) Chen, C. T.; Sette, F.; Ma, Y.; Hybertsen, M. S.; Stechel, E. B.; Foulkes, W. M. C.; Schulter, M.; Cheong, S.-W.; Cooper, A. S.; Rupp, L. W.; Batlogg, J. B.; Soo, Y. L.; Ming, Z. H.; Krol, A.; Kao, Y. H. Electronic states in $La_{2-x}Sr_xCuO_{4+\delta}$ probed by soft-x-ray absorption. *Phys. Rev. Lett.* **1991**, *66*, 104−107.

(60) Mizumaki, M.; Ishimatsu, N.; Kawamura, N.; Azuma, M.; Shimakawa, Y.; Takano, M.; Uozumi, T. Direct observation of the pressure-induced charge redistribution in $BiNiO_3$ by x-ray absorption spectroscopy. *Phys. Rev. B: Condens. Matter Mater. Phys.* **2009**, *80*, 233104.

(61) Yamada, I.; Etani, H.; Tsuchida, K.; Marukawa, S.; Hayashi, N.; Kawakami, T.; Mizumaki, M.; Ohgushi, K.; Kusano, Y.; Kim, J.; Tsuji, N.; Takahashi, R.; Nishiyama, N.; Inoue, T.; Irifune, T.; Takano, M. Control of Bond-Strain-Induced Electronic Phase Transitions in Iron Perovskites. *Inorg. Chem.* **2013**, *52*, 13751−13761.

(62) Long, Y. W.; Shimakawa, Y. Intermetallic charge transfer between A-site Cu and B-site Fe in A-site-ordered double perovskites. *New J. Phys.* **2010**, *12*, No. 063029.

(63) Long, Y. W.; Saito, T.; Tohyama, T.; Oka, K.; Azuma, M.; Shimakawa, Y. Intermetallic Charge Transfer in A-Site-Ordered Double Perovskite $BiCu_3Fe_4O_{12}$. *Inorg. Chem.* **2009**, *48*, 8489−8492.

(64) Yu, R. Z.; Hojo, H.; Watanuki, T.; Mizumaki, M.; Mizokawa, T.; Oka, K.; Kim, H.; Machida, A.; Sakaki, K.; Nakamura, Y.; Agui, A.; Mori, D.; Inaguma, Y.; Schlipf, M.; Rushchanskii, K. Z.; Ležaić, M.; Matsuda, M.; Ma, J.; Calder, S.; Isobe, M.; Ikuhara, Y.; Azuma, M. Melting of Pb Charge Glass and Simultaneous Pb−Cr Charge Transfer in $PbCrO_3$ as the Origin of Volume Collapse. *J. Am. Chem. Soc.* **2015**, *137* (39), 12719−12728.

(65) Murnaghan, F. D. The compressibility of media under extreme pressures. *Proc. Natl. Acad. Sci. U. S. A.* **1944**, *30* (9), 244−247.

(66) Birch, F. Finite elastic strain of cubic crystals. *Phys. Rev.* **1947**, *71*, 809−824.

(67) Yang, J. Y.; Terakura, C.; Medarde, M.; White, J. S.; Sheptyakov, D.; Yan, X. Z.; Li, N. N.; Yang, W. G.; Xia, H. L.; Dai, J. H.; Yin, Y. Y.; Jiao, Y. Y.; Cheng, J. G.; Bu, Y. L.; Zhang, Q. F.; Li, X. D.; Jin, C. Q.; Taguchi, Y.; Tokura, Y.; Long, Y. W. Pressure-induced spin reorientation and spin state transition in $SrCoO_3$. *Phys. Rev. B: Condens. Matter Mater. Phys.* **2015**, *92*, 195147.

(68) Vasala, S.; Karppinen, M. $A_2BB'O_6$ perovskites: A review. *Prog. Solid State Chem.* **2015**, *43*, 1−36.

https://dx.doi.org/10.1021/jacs.9b13508